AIAA AVIATION Forum
June 25-29, 2018, Atlanta, Georgia
2018 Fluid Dynamics Conference

10.2514/6.2018-4043

Approximating space-time flow statistics from a limited set of known correlations

Aaron Towne*, Xiang Yang†, Adrian Lozano-Durán*

We apply a method recently developed by Towne[1] for approximating space-time flow statistics from a limited set of measurements to a channel flow at friction Reynolds number $Re_\tau = 187$. The method uses the known data to infer the statistics of certain nonlinear terms that act as a forcing on the linearized Navier-Stokes equations, which in turn imply values for the unknown flow statistics through application of the resolvent operator. Using input data at a wall-normal position of $y^+ = 37$, accurate predictions of the velocity energy spectra and autocorrelations are obtained in the near-wall region, while significant under-predictions are observed further from the wall. Additional work is required to analyze the impact of the wall-normal location of the known input data and assess the performance of the method at higher Reynolds numbers.

I. Introduction

Practical limitations in both experiments and simulations can lead to partial knowledge of flow statistics. For example, an array of probes in an experiment provides information at a limited number of spatial locations and for a single flow quantity, e.g. velocity from hotwires or pressure from microphones. Similarly, particle image velocimetry might provide velocity data, but not thermodynamic quantities, in a limited field of view. In simulations, one may wish to know flow statistics in a region that is not adequately resolved by the computational grid, such as unresolved near-wall regions or locations outside of the main computational domain.

Towne[1] recently developed a method for estimating unknown space-time flow statistics from a limited set of known values. The method is based on the resolvent formalism of McKeon & Sharma.[2] The resolvent operator is derived from the Navier-Stokes equations linearized about the turbulent mean flow and constitutes a transfer function in the frequency domain between terms that are nonlinear and linear with respect to fluctuations to the mean. The basic idea of the method developed by Towne[1] is to use a limited set of known space-time flow statistics to infer the statistics of the nonlinear terms, which when fed through the resolvent operator imply values for the unknown flow statistics. This strategy depends on the close relationship between the resolvent operator and the cross-spectral density tensor shown by Towne *et al.*[3]

The method builds on the work of Beneddine *et al.*[4] and Zare *et al.*[5] These authors developed methods for completing unknown one-point temporal and two-point spatial statistics, respectively. These are both subsets of two-point space-time correlations, so our method can be thought of as a generalization or union of these previous approaches. This is an important step since two-point space-time statistics contain more information about the flow and constitute a starting point for identifying and modeling coherent structures.[3]

In this paper, we apply the method developed by Towne[1] to a turbulent channel flow at friction Reynolds number $Re_\tau = 187$. We take as known the space-time velocity statistics at a single wall-normal position $y/h = 0.2$ ($y^+ = 37$) and use the model to predict the flow statistics at other wall-normal locations. We show that the model provides accurate predictions of the velocity energy spectra and space-time autocorrelations for $y/h \lesssim 0.25$ ($y^+ \lesssim 45$). Larger errors are observed further from the wall, but the model predictions remain qualitatively reasonable. The success of the model in the near-wall region using knowledge of the interior flow suggests that it could be useful for designing new wall models for large-eddy simulation that are capable of capturing fluctuations of wall quantities such as shear stress and heat transfer and near-wall velocities that play an important role, for example, in particle laden flows.

*Center for Turbulence Research, Stanford University
†Department of Mechanical and Nuclear Engineering, Penn State University

The remainder of the paper is organized as follows. The method is described in section II and demonstrated in section III for a turbulent channel flow. Finally, Section IV summarizes the paper and discusses further improvements and applications of the method.

II. Method

II.A. Objective

We begin by reviewing the method introduced by Towne.[1] Consider a state-vector of flow variables $\boldsymbol{q}(\boldsymbol{x}, t)$ that describe a flow, e.g., velocities and thermodynamic variables. The independent variables $\boldsymbol{x}$ and t represent the spatial dimensions of the problem and time, respectively. Now suppose that the two-point space-time statistics are known for a reduced set of variables

$$\boldsymbol{y} = \mathcal{C}\boldsymbol{q}, \tag{1}$$

where the linear operator $\mathcal{C}(\boldsymbol{x})$ selects any desired subset or linear combination of $\boldsymbol{q}$. The problem objective can then be precisely stated in terms of two-point space-time correlation tensors:

$$\text{given} \qquad \boldsymbol{C_{yy}}(\boldsymbol{x}, \boldsymbol{x}', \tau) = E\left\{\boldsymbol{y}(\boldsymbol{x}, t)\boldsymbol{y}^*(\boldsymbol{x}', t+\tau)\right\}, \tag{2a}$$

$$\text{estimate} \qquad \boldsymbol{C_{qq}}(\boldsymbol{x}, \boldsymbol{x}', \tau) = E\left\{\boldsymbol{q}(\boldsymbol{x}, t)\boldsymbol{q}^*(\boldsymbol{x}', t+\tau)\right\}. \tag{2b}$$

Here, $E\left\{\cdot\right\}$ is the expectation operator and the asterisk superscript indicates a Hermitian transpose.

Using the relationship between space-time correlation tensors and the cross-spectral density tensors,

$$\boldsymbol{S}(\boldsymbol{x}, \boldsymbol{x}', \omega) = \int_{-\infty}^{\infty} \boldsymbol{C}(\boldsymbol{x}, \boldsymbol{x}', \tau) e^{i\omega\tau} d\tau, \tag{3}$$

this objective can be equivalently stated in the frequency domain:

$$\text{given} \qquad \boldsymbol{S_{yy}}(\boldsymbol{x}, \boldsymbol{x}', \omega) = E\left\{\hat{\boldsymbol{y}}(\boldsymbol{x}, \omega)\hat{\boldsymbol{y}}^*(\boldsymbol{x}', \omega)\right\}, \tag{4a}$$

$$\text{estimate} \qquad \boldsymbol{S_{qq}}(\boldsymbol{x}, \boldsymbol{x}', \omega) = E\left\{\hat{\boldsymbol{q}}(\boldsymbol{x}, \omega)\hat{\boldsymbol{q}}^*(\boldsymbol{x}', \omega)\right\}, \tag{4b}$$

where $\hat{\boldsymbol{y}}(\boldsymbol{x}, \omega)$ and $\hat{\boldsymbol{q}}(\boldsymbol{x}, \omega)$ are the Fourier transform of $\boldsymbol{y}$ and $\boldsymbol{q}$, respectively.

II.B. Approach

The approach to this problem developed by Towne[3] relies on the resolvent operator obtained from the linearized flow equations and its connection with the remaining nonlinear terms.[2] Begin with nonlinear flow equations of the form

$$\Gamma \frac{\partial \boldsymbol{q}}{\partial t} = \boldsymbol{\mathcal{F}}\left(\boldsymbol{q}\right). \tag{5}$$

The compressible Navier-Stokes equations are naturally written in this form with $\Gamma = I$, and the incompressible Navier-Stokes equations can be written this way by using a singular Γ to include the continuity equation. Additional transport equations can also be included.

Applying the Reynolds decomposition

$$\boldsymbol{q}\left(\boldsymbol{x}, t\right) = \bar{\boldsymbol{q}}\left(\boldsymbol{x}\right) + \boldsymbol{q}'\left(\boldsymbol{x}, t\right) \tag{6}$$

to equation (5) and isolating the terms that are linear in $\boldsymbol{q}'$ yields an equation of the form

$$\Gamma \frac{\partial \boldsymbol{q}'}{\partial t} - \mathcal{A}\left(\bar{\boldsymbol{q}}\right)\boldsymbol{q}' = \mathcal{B}\boldsymbol{f}\left(\bar{\boldsymbol{q}}, \boldsymbol{q}'\right), \tag{7}$$

where

$$\mathcal{A}\left(\bar{\boldsymbol{q}}\right) = \frac{\partial \boldsymbol{\mathcal{F}}}{\partial \boldsymbol{q}}\left(\bar{\boldsymbol{q}}\right) \tag{8}$$

is the linearized Navier-Stokes operator and $\boldsymbol{f}$ contains the remaining nonlinear terms. We have included the linear operator $\mathcal{B}$ to enable enforcement of known properties of the nonlinear terms in the ensuing analysis, e.g., that the forcing should not map onto the incompressible continuity equation since it is linear. Similarly, linearizing equation (1) yields

$$\boldsymbol{y}' = \mathcal{C}\boldsymbol{q}'. \tag{9}$$

In the frequency domain, equations (7) and (9) can be manipulated to give

$$\hat{\boldsymbol{y}} = \mathcal{R}_y \hat{\boldsymbol{f}}, \tag{10a}$$

$$\hat{\boldsymbol{q}} = \mathcal{R}_q \hat{\boldsymbol{f}}, \tag{10b}$$

where

$$\mathcal{R}_{\boldsymbol{y}}(\boldsymbol{x},\omega) = \mathcal{C}\left(i\omega\Gamma - \mathcal{A}\right)^{-1}\mathcal{B}, \tag{11a}$$

$$\mathcal{R}_{\boldsymbol{q}}(\boldsymbol{x},\omega) = \left(i\omega\Gamma - \mathcal{A}\right)^{-1}\mathcal{B}, \tag{11b}$$

are resolvent operators associated with $\hat{\boldsymbol{y}}$ and $\hat{\boldsymbol{q}}$, respectively.

Using equations (4) and (10), the cross-spectral density tensors can be written in terms of these resolvent operators as

$$\boldsymbol{S_{yy}} = \mathcal{R}_{\boldsymbol{y}} \boldsymbol{S_{ff}} \mathcal{R}_{\boldsymbol{y}}^*, \tag{12a}$$

$$\boldsymbol{S_{qq}} = \mathcal{R}_{\boldsymbol{q}} \boldsymbol{S_{ff}} \mathcal{R}_{\boldsymbol{q}}^*, \tag{12b}$$

where $\boldsymbol{S_{ff}}(\boldsymbol{x},\boldsymbol{x}',\omega) = E\{\hat{\boldsymbol{f}}(\boldsymbol{x},\omega)\hat{\boldsymbol{f}}^*(\boldsymbol{x}',\omega)\}$ is the cross-spectral density tensor of the nonlinear term $\boldsymbol{f}$.[3,6–8]

To obtain an approximation of the desired statistics $\boldsymbol{S_{qq}}$, we use the known statistics $\boldsymbol{S_{yy}}$ to estimate $\boldsymbol{S_{ff}}$. The salient question then becomes: how much can we learn about $\boldsymbol{S_{ff}}$ from $\boldsymbol{S_{yy}}$? An answer is provided by examining the singular value decomposition (SVD)

$$\mathcal{R}_{\boldsymbol{y}} = \boldsymbol{U_y}\boldsymbol{\Sigma_y}\boldsymbol{V_y}^* \tag{13a}$$

$$= \boldsymbol{U_y}\begin{bmatrix} \boldsymbol{\Sigma}_1 & \boldsymbol{0} \end{bmatrix}\left[\boldsymbol{V}_1 \;\; \boldsymbol{V}_2\right]^*. \tag{13b}$$

The columns of the matrices $\boldsymbol{V_y}$ and $\boldsymbol{U_y}$ correspond to input and output modes that form orthonormal bases for $\hat{\boldsymbol{f}}$ and $\hat{\boldsymbol{y}}$, respectively. The rectangular matrix $\boldsymbol{\Sigma_y}$ determines the gain of each of the input modes to the output. Since the rank of $\mathcal{R}_{\boldsymbol{y}}$ can be no greater than the number of entries in $\boldsymbol{y}$, i.e., the number of locations/quantities for which the statistics are known, many of the input modes have no impact on the output. Accordingly, the SVD can be written in the form of equation (13b), where the diagonal $\boldsymbol{\Sigma}_1$ contains the non-zero singular values and the blocks $\boldsymbol{V}_1$ and $\boldsymbol{V}_2$ contain input modes that have non-zero and zero gain, respectively. It is important to note that these resolvent modes are different from those usually studied, which are given by the SVD of $\mathcal{R}_{\boldsymbol{q}}$.

The distinction between input modes that do or do not impact the output can be used to isolate the part of $\boldsymbol{S_{ff}}$ that can be educed from knowledge of $\boldsymbol{S_{yy}}$. Since $\boldsymbol{V_y}$ provides a complete basis for $\hat{\boldsymbol{f}}$, $\boldsymbol{S_{ff}}$ can be expanded as

$$\boldsymbol{S_{ff}} = \left[\boldsymbol{V}_1 \;\; \boldsymbol{V}_2\right]\begin{bmatrix} \boldsymbol{E}_{11} & \boldsymbol{E}_{12} \\ \boldsymbol{E}_{21} & \boldsymbol{E}_{22} \end{bmatrix}\left[\boldsymbol{V}_1 \;\; \boldsymbol{V}_2\right]^*, \tag{14}$$

where the matrices $\boldsymbol{E}_{ij}$ represent correlation between expansion coefficients associated with each input mode.[3] Inserting this expansion into equation (12a) and using equation (13b) to simplify the expression leads to the equation

$$\boldsymbol{S_{yy}} = \boldsymbol{U_y}\boldsymbol{\Sigma}_1\boldsymbol{E}_{11}\boldsymbol{\Sigma}_1\boldsymbol{U_y}^*. \tag{15}$$

This means that only the part of $\boldsymbol{S_{ff}}$ associated with $\boldsymbol{E}_{11}$ impacts the observed statistics $\boldsymbol{S_{yy}}$; the remaining $\boldsymbol{E}_{ij}$ terms have no impact and are thus unobservable from this known data. Consequently, $\boldsymbol{E}_{11}$ contains all of the information about $\boldsymbol{S_{ff}}$ that can be inferred from $\boldsymbol{S_{yy}}$. Using the orthonormality of $\boldsymbol{U_y}$, equation (15) gives

$$\boldsymbol{E}_{11} = \boldsymbol{\Sigma}_1^{-1}\boldsymbol{U_y}^*\boldsymbol{S_{yy}}\boldsymbol{U_y}\boldsymbol{\Sigma}_1^{-1}. \tag{16}$$

The remaining terms $\boldsymbol{E}_{22}$ and $\boldsymbol{E}_{12} = \boldsymbol{E}_{21}^*$ (this equality is required to make $\boldsymbol{S_{ff}}$ Hermetian) can be arbitrarily chosen without impacting $\boldsymbol{S_{yy}}$, but these terms will impact $\boldsymbol{S_{qq}}$. The simplest choice, and the

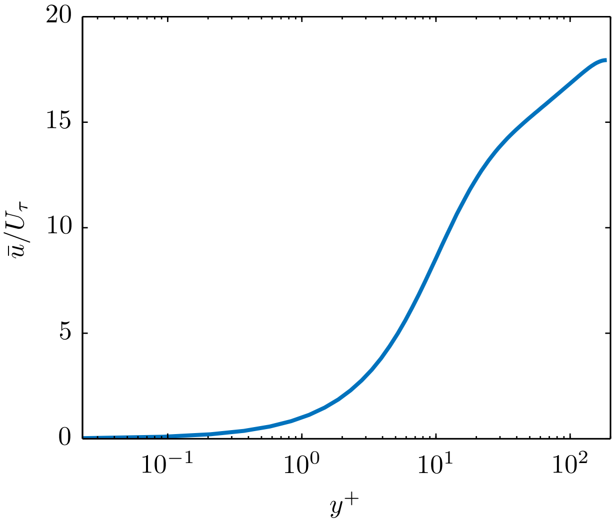

Figure 1: Mean velocity profile.

one used in the remainder of this paper, is to set these unknown terms to zero, leading to the approximation

$$\boldsymbol{S_{ff}} \approx [\boldsymbol{V}_1 \;\; \boldsymbol{V}_2] \begin{bmatrix} \boldsymbol{E}_{11} & 0 \\ 0 & 0 \end{bmatrix} [\boldsymbol{V}_1 \;\; \boldsymbol{V}_2]^* = \boldsymbol{V}_1 \boldsymbol{E}_{11} \boldsymbol{V}_1^*. \tag{17}$$

Inserting this into equation (12b) gives the corresponding approximation of the desired flow statistics,

$$\boldsymbol{S_{qq}} \approx \mathcal{R}_{\boldsymbol{q}} \boldsymbol{V}_1 \boldsymbol{E}_{11} \boldsymbol{V}_1^* \mathcal{R}_{\boldsymbol{q}}^*. \tag{18}$$

By construction, the known statistics used as input are exactly recovered, which ensures that the approximation converges in the limit of full knowledge of the flow statistics. Other approximations can be obtained by choosing the unknown $\boldsymbol{E}_{ij}$ terms differently; a few possibilities are discussed in Sec. IV.

III. Application to turbulent channel flow

III.A. Flow parameters and data processing

In this section, we apply the new method to an incompressible turbulent channel flow at friction Reynolds number $Re_\tau = 187$. The flow is computed via direct numerical simulation (DNS) in a domain of size $x/h \times y/h \times z/h \in [0, 2\pi] \times [0, 2] \times [0, \pi]$, where x, y, and z are the streamwise, wall-normal, and spanwise dimensions and h is the channel half-width. The periodic directions x and z are discretized using 64 Fourier modes in each direction, and the wall-normal direction y is discretized using 129 Chebyshev polynomials. The equations are advanced in time using a variable time step third-order Runge-Kutta integrator. To facilitate post processing, the data is interpolated in time to 10000 evenly spaced time instances. The mean streamwise velocity is shown in Figure 1.

The simulation data are used to compute the cross-spectral density tensor $\boldsymbol{S_{qq}}$, where $\boldsymbol{q} = [u, v, w]^T$ and u, v, and w are the streamwise, wall-normal, and spanwise velocities, respectively. Since the flow is periodic in x and z, the cross-spectral density is a function of wavenumber in these directions, i.e., $\boldsymbol{S_{qq}} = \boldsymbol{S_{qq}}(y, y'; k_x, k_z, \omega)$. The cross-spectral density is estimated using Welch's method.[9] The flow data are divided into overlapping blocks each containing N_{fft} instantaneous snapshots of the flow. A discrete Fourier transform in x, z, and t is applied to each block, leading to Fourier modes of the form $\hat{\boldsymbol{q}}_j(y; k_x, k_z, \omega)$ for $j = 1, 2, \ldots, N_b$, where N_b is the total number of blocks. Then, the cross-spectral density is estimated as

$$\boldsymbol{S_{qq}}(y, y'; k_x, k_z, \omega) = \frac{1}{N_b} \sum_{j=1}^{N_b} \hat{\boldsymbol{q}}_j(y; k_x, k_z, \omega) \hat{\boldsymbol{q}}_j^*(y'; k_x, k_z, \omega). \tag{19}$$

Finally, the estimated cross-spectra are further averaged according to the symmetries described by Sirovich,[10] which ensures that the estimated cross-spectra are symmetric with respect to reflection across the channel center line and to 180° rotation about the x-axis. We use blocks containing $N_{fft} = 256$ instantaneous snapshots with 75% overlap, leading to $N_b = 156$ blocks. We have verified that our results are insensitive to these choices.

III.B. Linearized Navier-Stokes equations

The resolvent operators required for the model are obtained from the incompressible Navier-Stokes equations

$$\frac{\partial \boldsymbol{u}}{\partial t} + \bar{\boldsymbol{u}} \cdot \nabla \boldsymbol{u} + \boldsymbol{u} \cdot \nabla \bar{\boldsymbol{u}} + \nabla p - \frac{1}{Re_\tau} \nabla \cdot \left[\frac{\nu_T}{\nu} \left(\nabla \boldsymbol{u} + \nabla \boldsymbol{u}^T \right) \right] = \boldsymbol{f_u}, \tag{20a}$$

$$\nabla \cdot \boldsymbol{u} = 0, \tag{20b}$$

where $\boldsymbol{u} = [u, v, w]^T$ is a vector of velocity disturbances, $\bar{\boldsymbol{u}} = [\bar{u}, 0, 0]$ is the mean velocity, and p is the pressure disturbance. Following Illingworth *et al.*,[11] we have included an eddy viscosity model in the form of the total viscosity function $\nu_T(y)$. Details can be found in that reference.

Since the linearized equations are homogeneous in x and z, we can apply Fourier transforms in these directions and obtain an equation for each (k_x, k_z) wavenumber pair in the form of equation (7) with

$$\mathcal{A} = ik_x A_x + A_y \frac{\partial}{\partial y} + ik_z A_z - k_x^2 A_{xx} + A_{yy} \frac{\partial^2}{\partial y^2} - k_z^2 A_{zz}, \tag{21}$$

$\Gamma = \text{diag}\left([1, 1, 1, 0]\right)$, and $\boldsymbol{q} = [u, v, w, p]^T$. The matrices in equation (21) are provided in the Appendix. The wall-normal direction y is discretized using 201 Chebyshev polynomials, and no-slip boundary conditions are applied at the walls.

We choose the known quantity $\boldsymbol{y}$ to correspond to the three velocity components at $y/h = 0.2$, which in inner units corresponds to $y^+ = 37$. This is the same y/h value considered by Illingworth *et al.*[11] in their recent Kalman filter study, although the y^+ value is different due to differing Reynolds numbers. This location is relevant to the application of LES wall modeling, in which one would use data along such a surface to approximate the near-wall flow and/or shear stress.

To visualize the results, we will focus on the velocity energy spectra, which are obtained from the cross-spectral density tensor as

$$\boldsymbol{E_{qq}}(y; k_x, k_z, \omega) = \boldsymbol{S_{qq}}(y, y; k_x, k_z, \omega). \tag{22}$$

III.C. Root-mean-squared velocities

We begin by examining the root-mean-squared (RMS) velocity fluctuations, which are obtained by integrating $\boldsymbol{E_{qq}}(y; k_x, k_z, \omega)$ in k_x, k_z, and ω and taking the square root. The true RMS velocity fluctuations computed from the DNS data and those obtained from the model are compared in Figure 2 as a function of y^+. The RMS values are accurately estimated for all three velocity components in the near-wall region, specifically for $y^+ \lesssim 45$ ($y/h \lesssim 0.25$). The streamwise velocity estimates are especially accurate, while slightly larger discrepancies are observed for the wall normal velocity. Notably, the model accurately captures both the location and magnitude of the u_{RSM} peak. For larger values of y^+, the RMS values quickly fall below the DNS values.

III.D. One-dimensional energy spectra

Figures 3, 4, and 5 show the energy spectrum for each velocity component as a function of y^+ and k_x^+, k_z^+, and ω^+, respectively. In each case, the energy has been integrated over the other two Fourier variables. The energies have been premultiplied by the appropriate wavenumber or frequency to account for the logarithmic axes. The contour levels are logarithmically spaced and span five orders of magnitude, with the highest level equal to the maximum value of the DNS streamwise velocity spectrum. The same levels are used in all subplots so that magnitudes can be directly compared. The true spectra computed from the DNS data appear in the top row of each figure, and the corresponding model estimates appear in the second row.

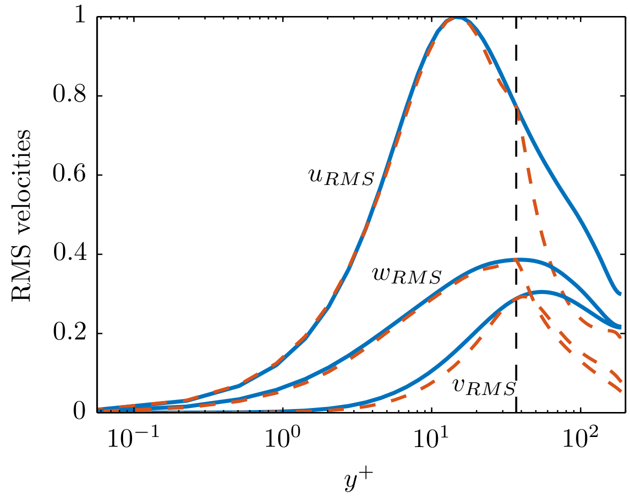

Figure 2: Root-mean-squared velocities, scaled by the maximum value of the streamwise component. Solid lines: true values calculated from the DNS data. Dashed lines: estimates obtained from the model using measurements at $y^+ = 37$ ($y/h = 0.2$). This input location is demarcated in the figure by the vertical dashed line.

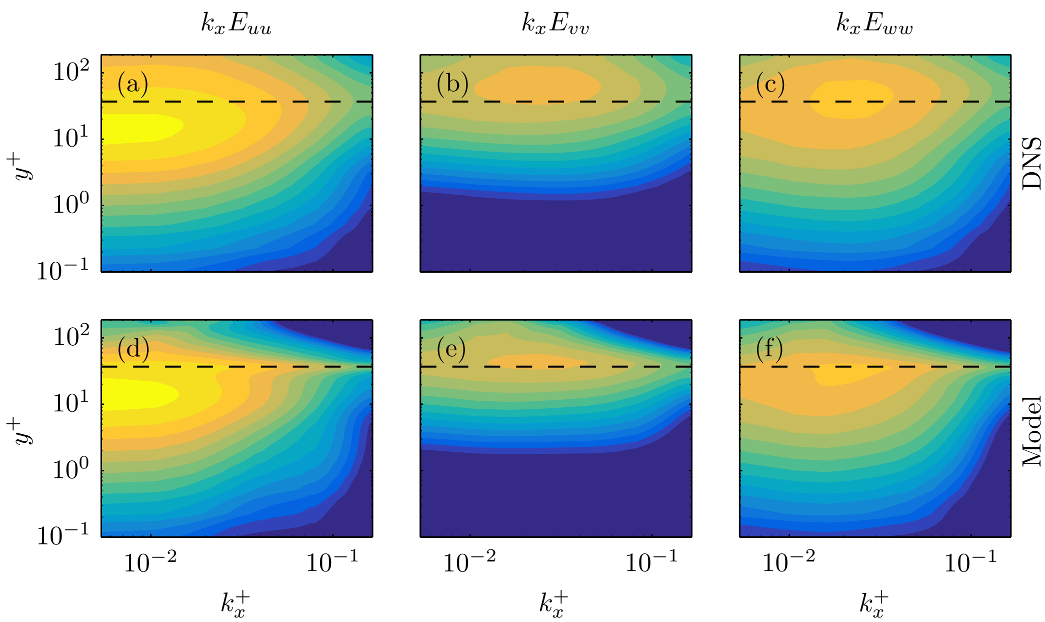

Figure 3: Premultiplied energy spectra as a function of streamwise wavenumber k_x^+ and wall-normal distance y^+. Top row: DNS. Bottom row: estimates from the model. Columns from left to right: streamwise velocity, wall-normal velocity, spanwise velocity. The contour levels are logarithmically spaced and span five orders of magnitude, with the highest level equal to the maximum value of the DNS streamwise velocity spectrum. The horizontal dashed lines show the location of the known input data, $y^+ = 37$.

In all cases, the model accurately captures the energy distribution of all three velocity components for $y^+ \lesssim 45$, except at the highest wavenumbers and frequencies. The amplitudes and locations of the energy peaks in $(y^+, k_x^+, k_z^+, \omega^+)$ space are captured by the model. On the other hand, the model under-predicts the energy at all wavenumbers and frequencies for higher values of y^+, which is consistent with the under-prediction of the RMS values observed in Figure 2. The highest wavenumbers and frequencies are correctly predicted only near the position of the known input data at $y^+ = 37$ (horizontal dashed lines in the figures).

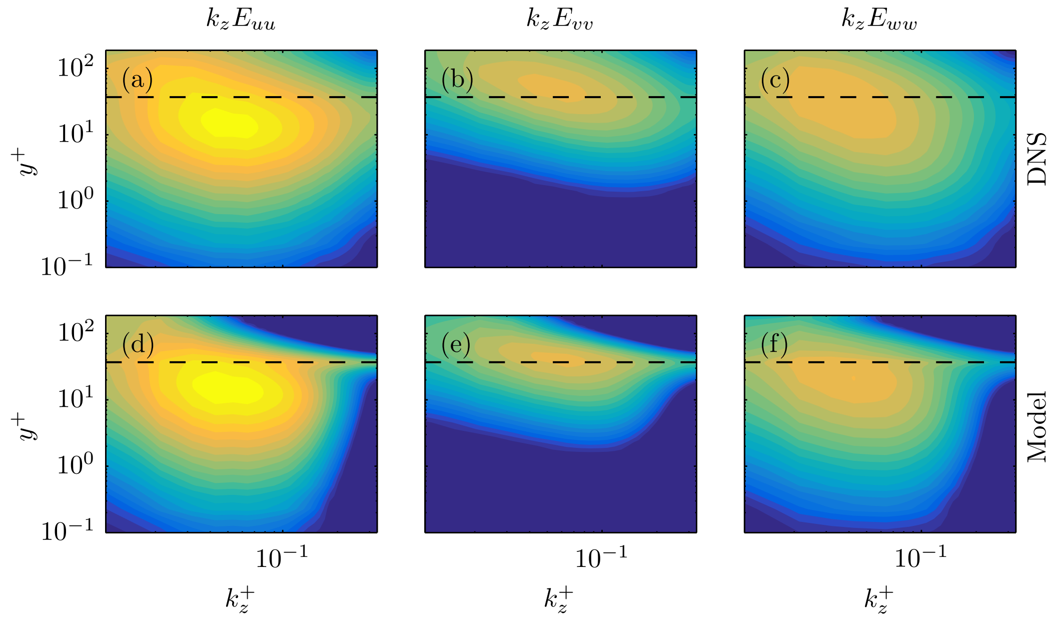

Figure 4: Premultiplied energy spectra as a function of spanwise wavenumber k_z^+ and wall-normal distance y^+. Top row: DNS. Bottom row: estimates from the model. Columns from left to right: streamwise velocity, wall-normal velocity, spanwise velocity. The contour levels are logarithmically spaced and span five orders of magnitude, with the highest level equal to the maximum value of the DNS streamwise velocity spectrum. The horizontal dashed lines show the location of the known input data, $y^+ = 37$.

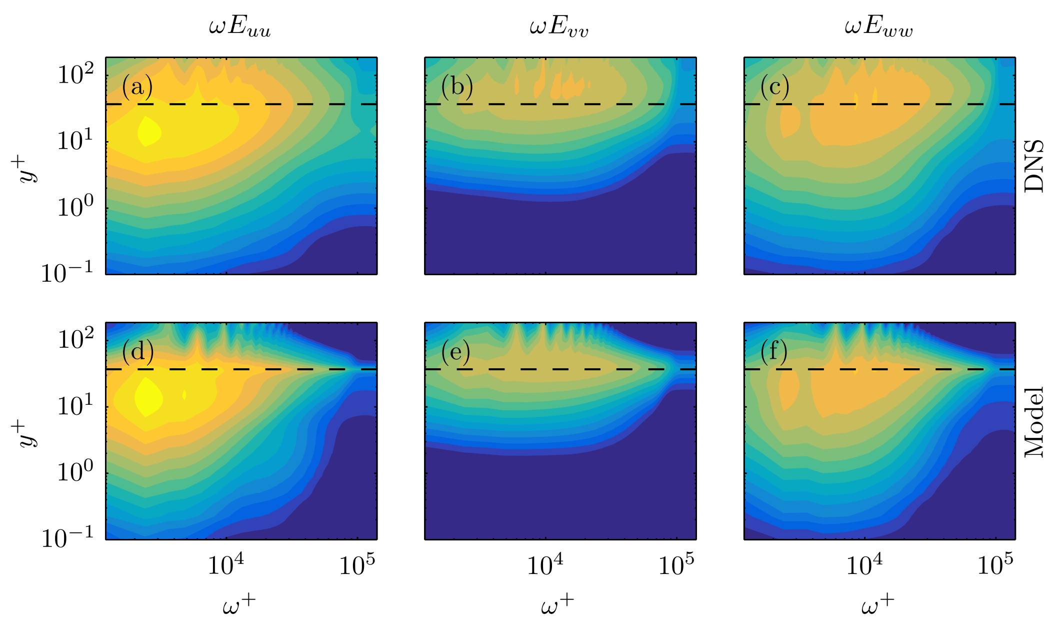

Figure 5: Premultiplied energy spectra as a function of frequency ω^+ and wall-normal distance y^+. Top row: DNS. Bottom row: estimates from the model. Columns from left to right: streamwise velocity, wall-normal velocity, spanwise velocity. The contour levels are logarithmically spaced and span five orders of magnitude, with the highest level equal to the maximum value of the DNS streamwise velocity spectrum. The horizontal dashed lines show the location of the known input data, $y^+ = 37$.

III.E. Two-dimensional energy spectra

Next, we consider two-dimensional energy spectra integrated over the remaining wavenumber or frequency at a fixed wall-normal location. Since we are primarily interested in near-wall behavior, we focus on the location $y/h = 0.05$, which corresponds to $y^+ = 9$.

Figure 6 shows the energy as a function of the streamwise and spanwise wavelengths λ_x^+ and λ_z^+. The contour levels are logarithmically distributed between 10% and 90% of the maximum value of the DNS spectrum for each component. The model provides good estimates of the energy distribution for all three velocity components. As before, the largest discrepancies are observed for the wall-normal velocity. From our observations in the last section, the differences between the DNS and modeled spectra can be largely attributed to an under-prediction of high frequency fluctuations.

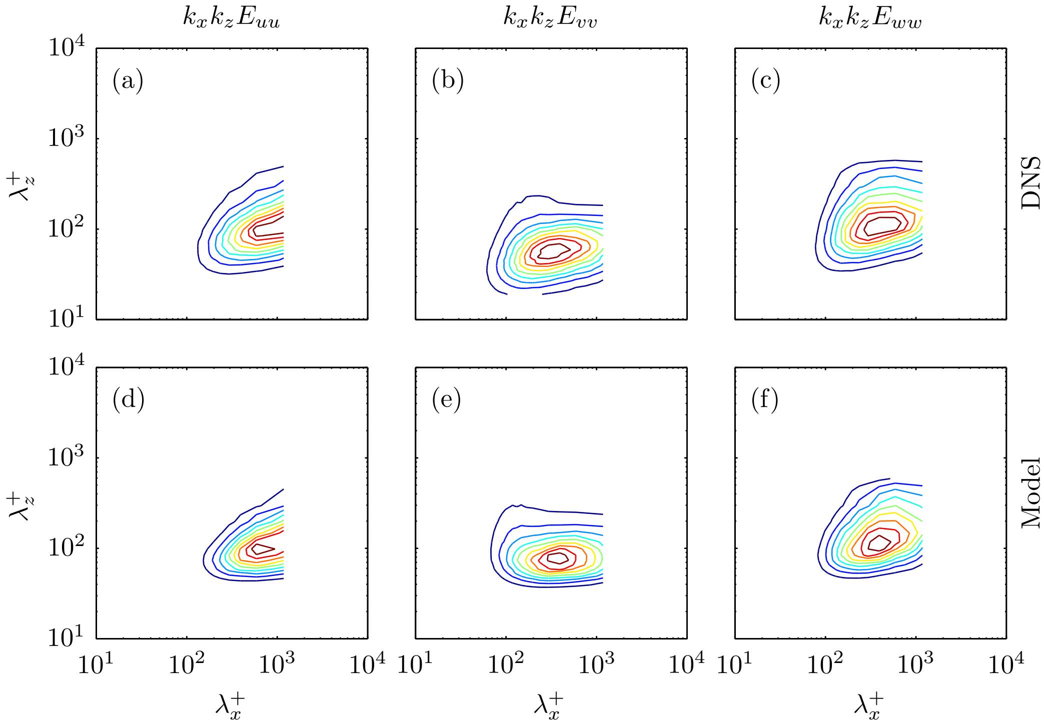

Figure 6: Premultiplied energy spectra as a function of streamwise wavelength λ_x^+ and spanwise wavelength λ_z^+ at $y^+ = 9$ ($y/h = 0.05$). Top row: DNS. Bottom row: estimates obtained from the model. Columns from left to right: streamwise, wall-normal, and spanwise velocity, respectively. The contour levels are logarithmically distributed between 10% and 90% of the maximum value of the DNS spectrum for each component.

Figure 7 shows the energy of each velocity component as a function of the streamwise wavenumber k_x and frequency ω. Here, we use linear axes so that the phase velocity $c_p = \omega/k_x$ can be easily visualized. The contour levels are logarithmically spaced between the maximum value of the streamwise spectrum from DNS and span five orders of magnitude. The same levels are used in all subplots.

Beginning with the DNS spectra shown in the top row, we see that the spectra are dominated by a band of energy that is approximately linear in $k_x - \omega$ space. The slope of this line corresponds to the phase velocity of the most energetic disturbances. At this wall-normal location, the dominant phase velocity is $c_p/U_\tau \approx 11$, which is shown as a dashed line in each subplot. The model accurately predicts the dominant phase velocity, and the main errors are observed primarily at phase velocities that are significantly different from the dominant one.

Figure 8 shows the $k_x - \omega$ spectra for the streamwise velocity at five different wall-normal locations: $y^+ = 2, 9, 19, 56, 94$ ($y/h = 0.01, 0.05, 0.1, 0.3, 0.5$). It is clear that the model correctly captures the changes in phase velocity as a function of wall-normal position, even when the absolute energy levels are under predicted.

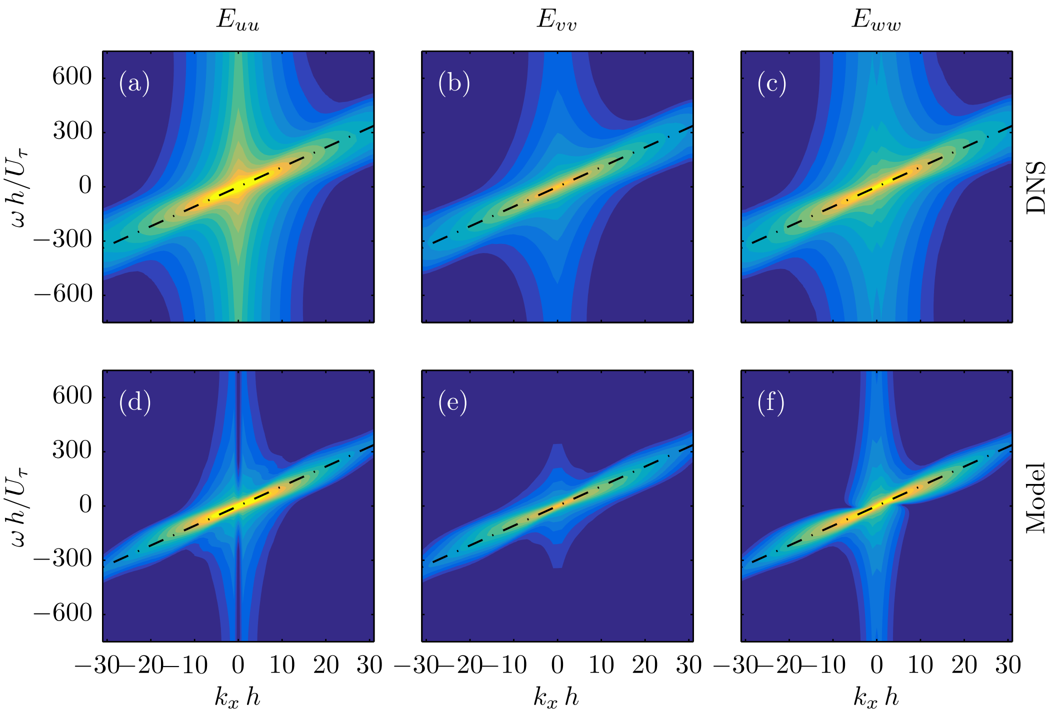

Figure 7: Energy spectra as a function of streamwise wavenumber k_x and frequency ω at $y^+ = 9$ ($y/h = 0.05$). Top row: DNS. Bottom row: estimates obtained from the model. Columns from left to right: streamwise, wall-normal, and spanwise velocity, respectively. The contour levels are logarithmically spaced and span five orders of magnitude, with the highest level equal to the maximum value of the DNS streamwise velocity spectrum. The dashed lines show the dominant phase speed at this wall-normal position.

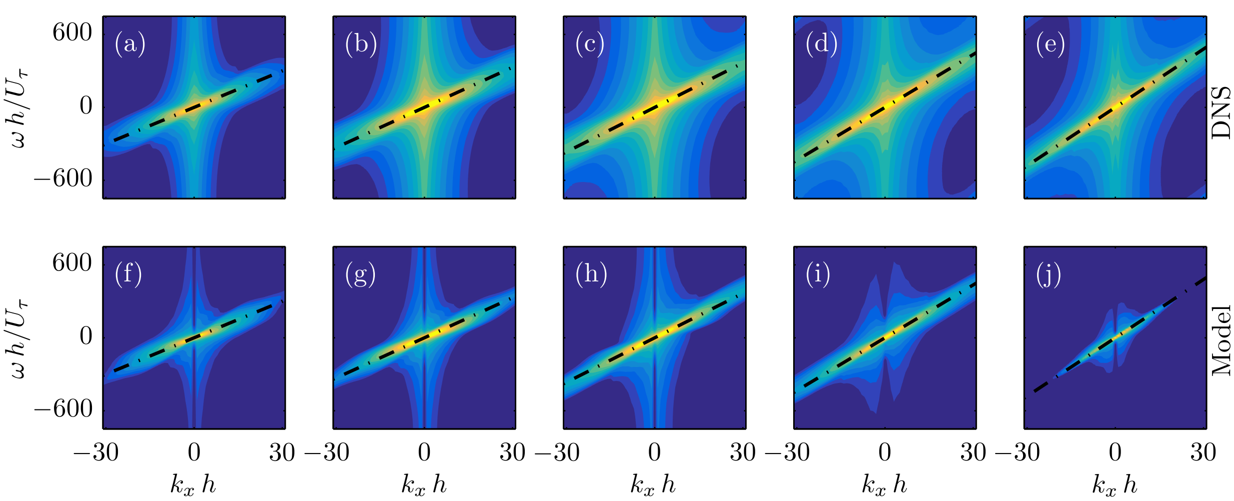

Figure 8: Streamwise velocity energy spectra as a function of streamwise wavenumber k_x and frequency ω at different wall-normal positions. Top row: DNS. Bottom row: estimates obtained from the model. Columns from left to right: $y^+ = 2, 9, 19, 56, 94$ ($y/h = 0.01, 0.05, 0.1, 0.3, 0.5$). The contour levels are logarithmically spaced and span five orders of magnitude, with the highest level equal to the maximum value of the DNS streamwise velocity spectrum at $y/h = 0.2$. The dashed lines show the dominant phase speed at each wall-normal position.

III.F. One-dimensional autocorrelations

Next, we consider the space-time correlations

$$\boldsymbol{C_{qq}}\left(y, y', \delta x, \delta z, \delta t\right) = E\left\{\boldsymbol{q}(x, y, z, t)\boldsymbol{q}^{*}(x+\delta x, y', z+\delta z, t+\delta t)\right\}, \tag{23}$$

where the expectation is taken over all x, z, and t. These correlations can be recovered from the cross-spectra discussed so far by taking inverse Fourier transforms,

$$\boldsymbol{C_{qq}}(y, y', \delta x, \delta z, \delta t) = \frac{1}{(2\pi)^3}\int_{-\infty}^{\infty}\int_{-\infty}^{\infty}\int_{-\infty}^{\infty}\boldsymbol{S_{qq}}(y, y', k_x, k_z, \omega)e^{-ik_x\delta x}e^{-ik_z\delta z}e^{-i\omega\delta t}dk_x dk_z d\omega. \tag{24}$$

We will focus on the autocorrelations

$$\boldsymbol{R_{qq}}\left(y; \delta x, \delta z, \delta t\right) = \boldsymbol{C_{qq}}\left(y, y, \delta x, \delta z, \delta t\right). \tag{25}$$

We begin by examining the autocorrelations as a function of y and one of the offsets δx, δz, or δt, with the other two set to zero. Figures 9, 10, and 11 show the autocorrelation for each velocity component as a function of y and δx, δz, and δt, respectively. The contour levels are linearly spaced between 90% and −20% of the maximum value of the autocorrelation of each velocity component computed from the DNS data. In all cases, the model accurately captures the autocorrelations for $y/h \lesssim 0.25$ and underestimates them for higher y/h values.

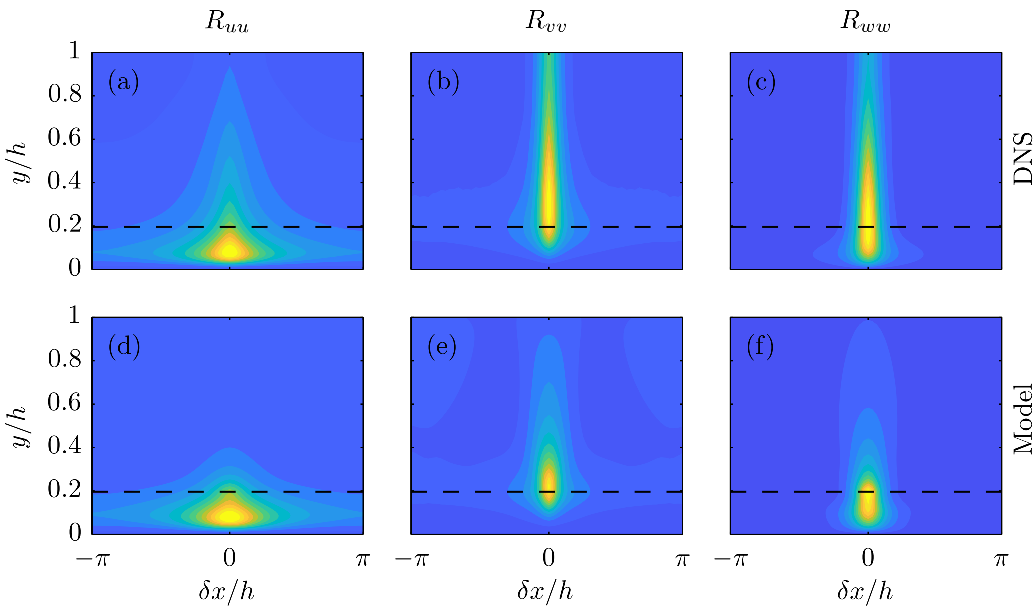

Figure 9: Autocorrelation as a function of streamwise separation δx and wall-normal position y. Top row: DNS. Bottom row: estimates obtained from the model. Columns from left to right: streamwise, wall-normal, and spanwise velocity, respectively. The contour levels are linearly spaced between 90% and −20% of the maximum value of the DNS autocorrelation of each velocity component.

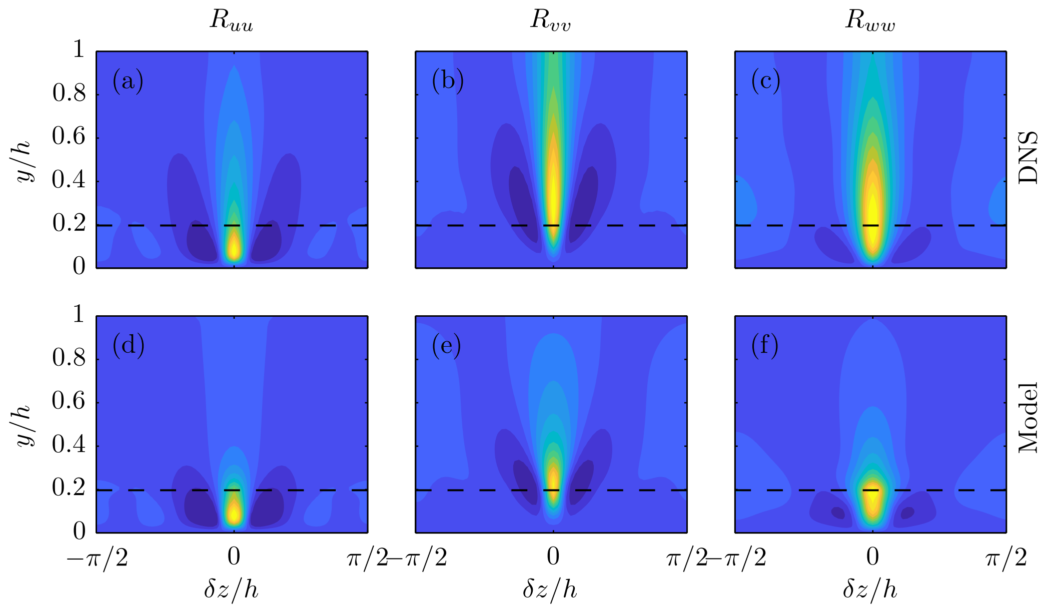

Figure 10: Autocorrelation as a function of spanwise separation δz and wall-normal position y. Top row:DNS. Bottom row: estimates obtained from the model. Columns from left to right: streamwise, wall-normal, and spanwise velocity, respectively. The contour levels are linearly spaced between 90% and −20% of the maximum value of the DNS autocorrelation of each velocity component.

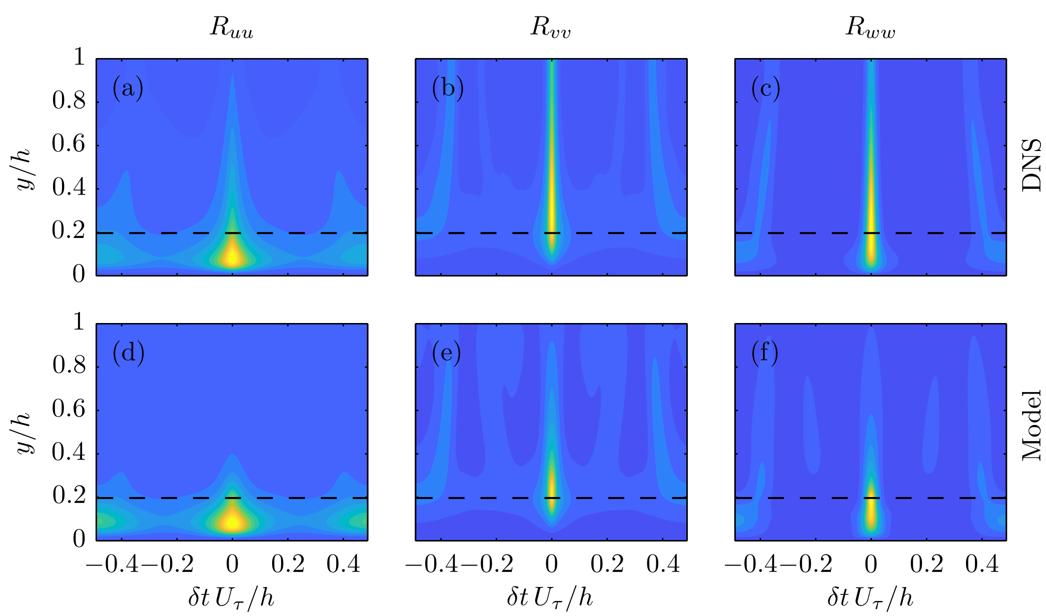

Figure 11: Autocorrelation as a function of temporal separation δt and wall-normal position y. Top row: DNS. Bottom row: estimates obtained from the model. Columns from left to right: streamwise, wall-normal, and spanwise velocity, respectively. The contour levels are linearly spaced between 90% and −20% of the maximum value of the DNS autocorrelation of each velocity component.

III.G. Two-dimensional autocorrelations

Finally, we examine the autocorrelations as a function of two of the lag variables δx, δz, and δt at a fixed wall-normal location y. As we did for the energy spectra, we focus on the location $y^+ = 9$ ($y/h = 0.05$).

Figure 12 shows the autocorrelation of each velocity component as a function of δx and δt, i.e., the space-time autocorrelations along the streamwise direction. The contour levels are defined in the same way as in the previous three figures. The inverse slope of the band of high correlation in each plot provides a measure of the convection velocity of disturbances. At this wall-normal location, the convection velocity is approximately $11U_\tau$, which is consistent with the phase velocity shown in Figure 7 as well as the observations of Kim & Hussain.[12] The convection velocity is accurately approximated by the model for all three velocity components. The correlation magnitudes are also well approximated aside from a moderate under prediction of the peak wall-normal velocity correlations.

Figure 13 shows the autocorrelations as a function of δx and δz for $y^+ = 9$ ($y/h = 0.05$). The model provides accurate predictions for all three velocity components.

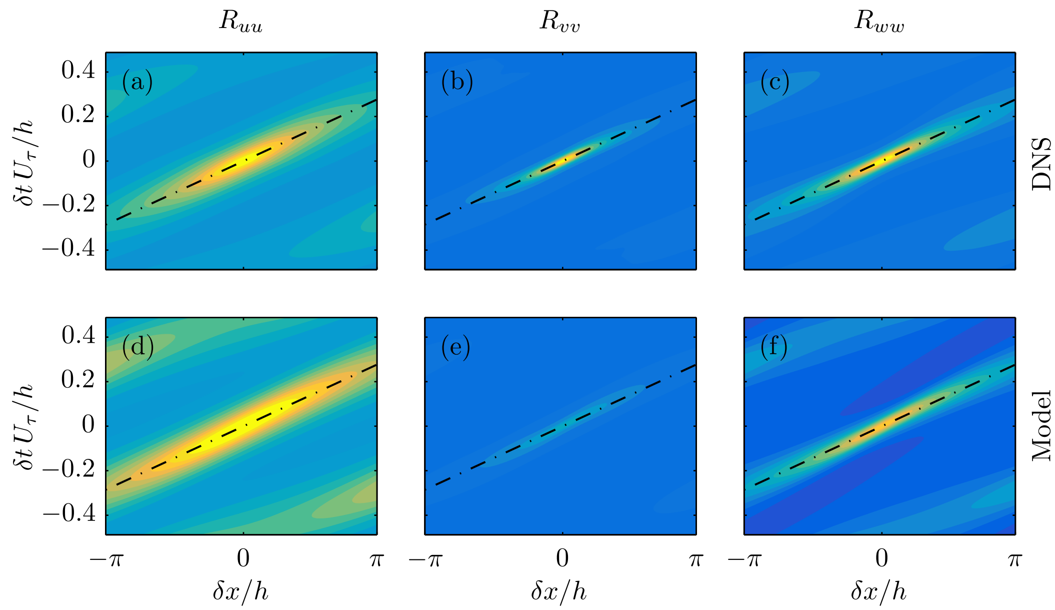

Figure 12: Autocorrelation as a function of streamwise separation δx and temporal separation δt at $y^+ = 9$ ($y/h = 0.05$). Top row: DNS. Bottom row: estimates obtained from the model. Columns from left to right: streamwise, wall-normal, and spanwise velocity, respectively. The contour levels are linearly spaced between 90% and −20% of the maximum value of the DNS autocorrelation of each velocity component. The slope of the dashed lines give the inverse of the dominant convection velocity.

IV. Conclusions

Towne[1] recently introduced a new method for completing partially know space-time flow statistics. The method is based on the resolvent methodology developed by McKeon & Sharma[2] and builds on the work of Beneddine *et al.*,[4] Zare *et al.*,[5] and Towne *et al.*[3] The central idea of the approach is to use known data to infer the statistics of the nonlinear terms that constitute a forcing on the linearized Navier-Stokes equations. These forcing statistics then imply values for the remaining unknown flow statistics through application of the resolvent operator.

In this paper, we have applied this method to a real turbulent flow for the first time, namely a turbulent channel at friction Reynolds number $Re_\tau = 187$. Using data exclusively from the wall-normal location $y/h = 0.2$ ($y^+ = 37$), the method provides good estimates of the velocity energy spectra and autocorrelations for $y \lesssim 0.25$ ($y^+ \lesssim 45$). The energies and autocorrelations are under-predicted further away from the wall. In general, the wall-normal velocity statistics are predicted less accurately than the other two velocity components.

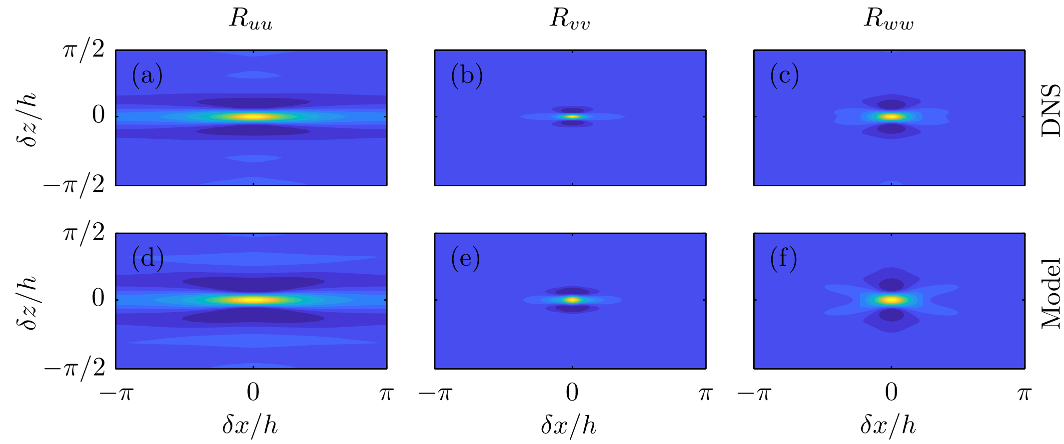

Figure 13: Autocorrelation as a function of streamwise separation δx and spanwise separation δz at $y^+ = 9$ ($y/h = 0.05$). Top row: DNS. Bottom row: estimates obtained from the model. Columns from left to right: streamwise, wall-normal, and spanwise velocity, respectively. The contour levels are linearly spaced between 90% and -20% of the maximum value of the DNS autocorrelation of each velocity component.

Further work is required to understand these observations, assess the impact of the location of the known input data, and determine whether the results described in this paper will extend to higher Reynolds numbers. The properties and performance of the method should also be directly compared to other approaches that use the linearized flow equations as the basis for flow estimation, including the recent Kalman-filter-based approach described by Illingworth *et al.*[11]

Additionally, the method itself could be further improved by modeling the portions of the forcing cross-spectral density that can not be observed using the known data. In the current formulation, these terms are simply set to zero, and there exist several possible alternatives. One is to assume that the unobserved forcing is uncorrelated with the observed part and with itself, leading to the approximation

$$\boldsymbol{S_{ff}} = [\boldsymbol{V}_1 \;\; \boldsymbol{V}_2] \begin{bmatrix} \boldsymbol{E}_{11} & 0 \\ 0 & a\boldsymbol{I} \end{bmatrix} [\boldsymbol{V}_1 \;\; \boldsymbol{V}_2]^* . \tag{26}$$

An appropriate value for the scalar amplitude a could be determined from the amplitudes of the know $\boldsymbol{E}_{11}$ terms. Another possibility is to choose the unobservable terms by insisting that the estimated $\boldsymbol{S_{ff}}$ projects exclusively onto the first n singular modes of $\mathcal{R}_y$. The $\boldsymbol{E}_{ij}$ values that achieve this can be obtained using simple linear algebra manipulations. This possibility is similar to a suggestion made by Beneddine *et al.*,[13] except here the expansion coefficients are treated as statistical quantities rather than complex scalars. As shown by Towne *et al.*,[3] this statistical treatment removes a fundamental accuracy restriction imposed by treating the expansion coefficients as deterministic scalars and allows for a convergent approximation.

Acknowledgments

This investigation was funded by the NNSA Predictive Science Academic Alliance Program II, grant no. DE-NA0002373.

Appendix: Linearized incompressible Navier-Stokes operators

The matrices defining the linearized incompressible Navier-Stokes equations in equations (7) and (21) are:

$$\boldsymbol{A}_x = \begin{bmatrix} \bar{u} & -\nu'_T & 0 & 1 \\ 0 & \bar{u} & 0 & 0 \\ 0 & 0 & \bar{u} & 0 \\ 1 & 0 & 0 & \bar{u} \end{bmatrix}, \quad \boldsymbol{A}_y = \begin{bmatrix} -\nu'_T & 0 & 0 & 0 \\ 0 & -2\nu'_T & 0 & 1 \\ 0 & 0 & -\nu'_T & 0 \\ 0 & 1 & 0 & 0 \end{bmatrix}, \quad \boldsymbol{A}_z = \begin{bmatrix} 0 & 0 & 0 & 0 \\ 0 & 0 & 0 & 0 \\ 0 & 0 & 0 & 1 \\ 0 & -\nu'_T & 1 & 0 \end{bmatrix},$$

$$\boldsymbol{A}_0 = \begin{bmatrix} 0 & \frac{\partial \bar{u}}{\partial y} & 0 & 0 \\ 0 & 0 & 0 & 0 \\ 0 & 0 & 0 & 0 \\ 0 & 0 & 0 & 0 \end{bmatrix}, \quad \boldsymbol{\Gamma} = \begin{bmatrix} 1 & 0 & 0 & 0 \\ 0 & 1 & 0 & 0 \\ 0 & 0 & 1 & 0 \\ 0 & 0 & 0 & 0 \end{bmatrix}, \quad \boldsymbol{B} = \begin{bmatrix} 1 & 0 & 0 \\ 0 & 1 & 0 \\ 0 & 0 & 1 \\ 0 & 0 & 0 \end{bmatrix},$$

and $\boldsymbol{A}_{xx} = \boldsymbol{A}_{yy} = \boldsymbol{A}_{zz} = -\frac{1}{Re}\boldsymbol{\Gamma}$. We have defined $\nu'_T = \frac{1}{Re}\frac{\partial \nu_T}{\partial y}$.

References

[1] Towne, A., "Completing partially known space-time flow statistics: a resolvent-based approach," *Annual Research Briefs*, Center for Turbulence Research, Stanford University, 2017.

[2] McKeon, B. J. and Sharma, A. S., "A critical-layer framework for turbulent pipe flow," *J. Fluid Mech.*, Vol. 658, 2010, pp. 336–382.

[3] Towne, A., Schmidt, O. T., and Colonius, T., "Spectral proper orthogonal decomposition and its relationship to dynamic mode decomposition and resolvent analysis," *arXiv:1708.04393*, 2017.

[4] Beneddine, S., Sipp, D., Arnault, A., Dandois, J., and Lesshafft, L., "Conditions for validity of mean flow stability analysis," *J. Fluid Mech.*, Vol. 798, 2016, pp. 485–504.

[5] Zare, A., Jovanović, M. R., and Georgiou, T. T., "Colour of turbulence," *J. Fluid Mech.*, Vol. 812, 2017, pp. 636–680.

[6] Towne, A., Colonius, T., Jordan, P., Cavalieri, A. V. G., and Brès, G. A., "Stochastic and nonlinear forcing of wavepackets in a Mach 0.9 jet," *AIAA Paper #2015-2217*, 2015.

[7] Semeraro, O., Jaunet, V., Jordan, P., Cavalieri, A. V. G., and Lesshafft, L., "Stochastic and harmonic optimal forcing in subsonic jets," *AIAA Paper #2016-2935*, 2016.

[8] Towne, A., Brès, G. A., and Lele, S. K., "Toward a resolvent-based statisitical jet-noise model," *Annual Research Briefs*, Center for Turbulence Research, Stanford University, 2016.

[9] Welch, P., "The use of fast Fourier transform for the estimation of power spectra: a method based on time averaging over short, modified periodograms," *IEEE Trans. Audio Electroacoust.*, Vol. 15, No. 2, 1967, pp. 70–73.

[10] Sirovich, L., "Turbulence and the dynamics of coherent structures. II. Symmetries and transformations," *Quart. Appl. Math.*, Vol. 45, No. 3, 1987, pp. 573–582.

[11] Illingworth, S. J., Monty, J. P., and Marusic, I., "Estimating large-scale structures in wall turbulence using linear models," *J. Fluid Mech.*, Vol. 842, 2018, pp. 146162.

[12] Kim, J. and Hussain, F., "Propagation velocity of perturbations in turbulent channel flow," *Phys. Fluids*, Vol. 5, No. 3, 1993, pp. 695–706.

[13] Beneddine, S., Yegavian, R., Sipp, D., and Leclaire, B., "Unsteady flow dynamics reconstruction from mean flow and point sensors: an experimental study," *J. Fluid Mech.*, Vol. 824, 2017, pp. 174–201.